

1 **Trends of the high latitude mesosphere temperature and mesopause**
2 **revealed by SABER**

3 **Xiao Liu^{1,2}, Jiyao Xu^{2,3}, Jia Yue^{4,5}, Yangkun Liu^{1,2}, and Vania F. Andrioli^{2,6}**

4 ¹Institute of Electromagnetic Wave, School of Physics, Henan Normal University, Xinxiang,
5 453000, China

6 ²State Key Laboratory of Space Weather, National Space Science Center, Chinese Academy of
7 Sciences, Beijing, 100190, China

8 ³School of Astronomy and Space Science, University of the Chinese Academy of Science, Beijing,
9 100049, China

10 ⁴Catholic University of America, Washington, DC 20064, USA

11 ⁵NASA Goddard Space Flight Center, Greenbelt, MD, 20771, USA

12 ⁶Heliophysics, Planetary Science and Aeronomy Division, National Institute for Space Research
13 (INPE), Sao Jose dos Campos, Sao Paulo, Brazil

14

15 *Correspondence to: Jiyao Xu (xujy@nssc.ac.cn)*

16

17 **Key Points:**

- 18 • The mean temperature in the high latitude MLT region is obtained by binning the SABER
19 observations based on yaw cycles during 2002–2023
- 20 • In the high latitude MLT, the cooling trend is seasonal symmetric and reaches peak of ≥ 6
21 K/decade at highest latitudes around summer solstice
- 22 • The trends of mesopause temperature depend on latitudes but are mostly negative and have
23 larger magnitudes at highest latitude

24

25

26 **Abstract**

27 The temperature trend in the mesosphere and lower thermosphere (MLT) region can be
28 regarded as an indicator of climate change. Using temperature profiles measured by the Sounding of
29 the Atmosphere using Broadband Emission Radiometry (SABER) instrument during 2002–2023
30 and binning them based on yaw cycle, we get continuous dataset with wide local time coverage at
31 50°S–80°N or 80°S–50°N. The seasonal change of temperature, caused by the forward drift of
32 SABER yaw cycle, is removed by using the climatological temperature of MSIS2.0. The corrected
33 temperature without any waves ~~and~~ is regarded as the mean temperature. At 50°S–50°N, the cooling
34 trends of the mean temperature are significant in the MLT region and are in agreement with
35 previous studies. The novel finding is that the cooling trends of ≥ 2 K/decade exhibit seasonal
36 symmetric and reach peaks of ≥ 6 K/decade at ~~high~~^{est} latitudes around the summer solstice.
37 Moreover, there are warming trends of 1–2.5 K/decade at ~~pressure height~~^{altitude} range of 10^{-2} – 10^{-3}
38 hPa, specifically at latitudes higher than 55°N in October and December and at latitudes higher than
39 55°S in April and August. The mesopause temperature (~~height~~^{altitude}) in the northern summer polar
40 region is colder (lower) than that in the southern counterpart by ~5–11 K (~1 km) over the past 22
41 years. The trends of the mesopause temperature are dependent on latitudes and months. But they are
42 negative at most latitudes and reach larger magnitudes at ~~high~~^{est} latitudes. These results indicate
43 that the temperature in ~~the~~ high latitude MLT region is more sensitive to dynamic changes.

44

45 **1 Introduction**

46 Observational and simulation studies have revealed that the global mean temperature trend is
47 cooling in the mesosphere and lower thermosphere (MLT) (Beig et al., 2003; Laštovička et al.,
48 2006; Yue et al., 2019b; Laštovička, 2023). The cooling trends observed in the MLT region are
49 mainly caused by the increasing anthropogenic greenhouse gases such as carbon dioxide. Moreover,
50 changes of the stratospheric ozone depletion and recovery, increasing mesospheric water vapor
51 concentration, solar and geomagnetic variations may also contribute to the long-term changes of
52 temperature in the MLT region (Laštovička, 2009; Yue et al., 2019a, 2015; Garcia et al., 2019;
53 Mlynczak et al., 2022; Zhang et al., 2023).

54 A recent review work by Laštovička (2023) summarized that temperature trends are generally
55 cooling but also depend on local times, heights, and geographic locations in the MLT region
56 (Venkat Ratnam et al., 2019; Das, 2021; She et al., 2019; Yuan et al., 2019; Ramesh et al., 2020).
57 These results were mostly derived from ground-based and satellite observations at low and middle
58 latitudes, while the simulations provided insights into the long-term trends from pole to pole. On the
59 other hand, the long-term trends in temperature at high latitudes have not been thoroughly examined
60 and well understood yet, due to scarce observations. Driven by the summer-to-winter meridional
61 circulation, the upwelling causes adiabatic cooling in the summer polar mesosphere, while the
62 downwelling causes adiabatic warming in the winter polar mesosphere (Dunkerton, 1978; Garcia
63 and Solomon, 1985). Thus, the high latitude temperature is more sensitive to the changes of
64 dynamics, wave and forcing, stratospheric wind etc. (Russell et al., 2009; Qian et al., 2017; Yu et
65 al., 2023).

66 The progress in studying long-term trends in the MLT region has been summarized and
67 reported by Laštovička and Jelínek (2019) and Laštovička (2023). Here we highlight some studies
68 related to the temperature trends ~~in temperature~~ at high latitudes. Using temperature measured by
69 the Sounding of the Atmosphere using Broadband Emission Radiometry (SABER) instrument and
70 simulated by Whole Atmosphere Community Climate Model version 4 (WACCM4), Garcia et al.
71 (2019) showed that the global mean SABER temperature (52°S–52°N) ~~had of a~~ cooling trends s of
72 0.4–0.5 K/decade during 2002–2018 in the stratosphere and mesosphere. ~~-. These magnitudes~~ were
73 smaller than those simulated by WACCM4 (0.6–0.9 K/decade) but within 2 times of the standard
74 deviation. Using Leibniz Institute Middle Atmosphere Model (LIMA) under northern hemispheric
75 conditions during 1871–2008, Lübken et al. (2018) showed that the cooling trend in the MLT region
76 was 1.5 K/decade during 1960–2008, and was 0.7 K/decade during 1871–2008 at 55–61°N on
77 geometric heights. However, the trend was neglectable on pressure heights. On pressure heights, the
78 global mean SABER temperature (55°S–55°N) had cooling trends of 0.5 and 2.6 K/decade,
79 respectively, at 10^{-3} hPa (~92 km) and 10^{-4} hPa (~106 km) during 2002–2021 (Mlynczak et al.,

80 2022). The results of Lübken et al. (2018) and Mlynczak et al. (2022) illustrated that the cooling
81 trends were larger over recent decades on both geometric and pressure heights as compared to the
82 beginning of industrialization. To achieve a longer time series, Li et al. (2021) constructed a nearly
83 30-year dataset at 45°S–45°N by merging the temperature measured by the Halogen Occultation
84 Experiment (HALOE) instrument during 1991–2005 and the SABER instrument during 2002–2019.
85 They showed that the cooling trend was significant and reached a peak of 1.2 K/decade at 60–70 km
86 in the Southern Hemisphere (SH) tropical and subtropical region. Moreover, the cooling trend in the
87 SH was larger than its counterpart in the Northern Hemisphere (NH).

88 At high latitudes, ground-based observations of OH nightglow rotational temperature revealed
89 a significant cooling trend of 1.2 ± 0.51 K/decade at Davis (68°S, 78°E) during 1995–2019 (French
90 et al., 2020). The OH rotational temperature around midnight exhibited a significant cooling trend
91 of $2.4 \text{ K} \pm 2.3$ /decade in summer and an insignificant cooling trend of 0.4 ± 2.2 K/decade in winter
92 at Moscow (57°N, 37°E) during 2000–2018 (Dalin et al., 2020). Using the ice layer parameters
93 simulated by the LIMA model and the Mesospheric Ice Microphysics And transport ice particle
94 model, Lübken et al. (2021) showed that the negative trend of noctilucent clouds ~~heights-altitudes~~
95 (~83 km) was primarily caused by ~~the increasing CO₂-induced cooling at lower heights in the~~
96 ~~troposphere~~ during 1871–2008 at 58°N, 69°N, and 78°N. At these three latitudes, the cooling trends
97 were of ~0.2 K/decade during 1871–1960 and 1.0 K/decade during 1960–2008. Near the latitude
98 band of 64–70°N in June and 64–70°S in December, Bailey et al. (2021) constructed two datasets
99 by merging the temperature measured by HALOE and SABER and by HALOE and SOFIE (Solar
100 Occultation for Ice Experiment). They showed that there were cooling trends of ~1–2 K/decade near
101 0.1–0.01 hPa (~68–80 km) and warming trends of ~1 K/decade near 0.005 hPa (~85 km) at 64–
102 70°N in June and 64–70°S in December. Moreover, the WACCM-X simulation results by Qian et al.
103 (2019) showed that the temperature trends were mostly cooling in the MLT region. However, there
104 were also warming at ~80–95 km in the SH polar region from November to February (Fig. 3 of
105 their paper). The disagreement of these results at high latitudes might attribute to the different
106 temporal spans and local times, observations using different instruments, and different methods
107 deriving the trends. It is overarching to study the temperature trends at high latitudes using one
108 coherent measurement over a long period.

109 The SABER temperature profiles cover latitudes of 53°S–83°N in the north viewing
110 maneuvers and 83°S–53°N in the south viewing maneuvers since 2002. ~~The operational SABER~~
111 ~~temperature profile covers an altitude range of ~15–110 km. The uncertainties of SABER~~
112 ~~temperature profile are height dependent. For a single temperature profile, its uncertainties are~~
113 ~~summarized at <https://spdf.gsfc.nasa.gov/pub/data/timed/saber/> and are of ~1.8–2.3 K at z=60–80~~
114 ~~km, ~5.4–8.4 K at 90–100 km, and ~8.4–29.2 K at 100–110 km under the condition of Each~~

115 ~~temperature profile covers a height range of ~15–110 km with accuracies of ~1.8–2.3 K at z=60–80~~
116 ~~km and ~5.4–8.4 K at 90–100 km and~~ vertical resolution of 2 km (Remsberg et al., 2008; Rezac et
117 al., 2015; Dawkins et al., 2018). These data exhibited remarkable stability over the last two decades
118 following the correction of algorithm instability (Mlynczak et al., 2020, 2022, 2023). Using the
119 SABER temperature profiles during 2002–2019, Zhao et al. (2020) employed a 60-day moving
120 window to obtain the mean temperature. Their analysis revealed that the annual and global mean
121 trend of mesopause temperature is cooling with magnitude of 0.75 K/decade. Moreover, the cooling
122 trend is significant in non-summer seasons but insignificant in summer (May–August) at 60–
123 80°N/S. It should be noted that, SABER yaw cycle (YC) drifted forward about one month from
124 2002 to 2023 (see Fig. 1 below) due to changing satellite orbit. This induces the local time (LT)
125 coverage in a certain month differing from year to year at high latitudes if the window is set to be
126 constantly 60-days.

127 Here we focus on the trend of the mean temperature without any atmospheric waves (i.e.,
128 gravity waves, tides and planetary waves). Calculating zonal mean can remove gravity waves,
129 nonmigrating tides and long-period planetary waves. However, migrating tides depend on LT and
130 are strong in the MLT region. They cannot be simply removed by calculating zonal mean. In this
131 work, we bin the data based on YC, which covers an interval of 54–64 days (see Fig. 1 below) and
132 provides almost full local time coverage (except the 1–3 hours around noon). Thus, the mean
133 temperature can be accurately determined by removing the migrating tides at 53°S–83°N or 83°S–
134 53°N using harmonic fitting. Each YC at every year covers varying ranges of dates. This results in
135 the aliasing of the seasonal variation of temperature into the mean temperature of each YC. This
136 issue can be resolved as below. We use the temperature of the recently released whole-atmosphere
137 empirical model MSIS2.0 (Emmert et al., 2021) as a reference for the seasonal variation. This
138 seasonal variation (more than 10 K as seen in Fig. 2b) embedded in YC drift is removed from the
139 mean temperature of each YC. Thus, using the advantages of SABER measurements at high
140 latitudes and binning the data based on YC, we focus on the long-term trends of the mean
141 temperature and the mesopause in the high latitude MLT region.

142 **2 Method of calculating mean temperature and trend**

143 The mean temperature (\bar{T}_{bk}) excludes gravity wave, tides and planetary waves. Moreover,
144 compared to the magnitudes of \bar{T}_{bk} , its trend is a small value and should be determined with extra
145 caution. The method of calculating \bar{T}_{bk} is based on a YC window. This ensures a good LT coverage
146 at high latitudes. Compared to the fixed 60-day window, the advantage and necessity of the YC
147 window are described below.

148 The YC window is defined as the temporal interval during which the SABER measurements

149 are in the northward or southward viewing maneuver. Figure 1 shows the beginning date and
 150 temporal span of each YC. We see that there are about six YCs in each year, being named as YC1–
 151 YC6. The temporal spans of YCs are 54–64 days. This ensures that the LT coverage of SABER
 152 samplings is more than 18 hours at high latitudes. Therefore, migrating tides can be removed
 153 efficiently through harmonic fitting. In contrast, the LT coverage in a fixed 60-day window is
 154 different from year to year at high latitudes. This is because the temporal span of each YC drifted
 155 forward about one month from 2002 to 2023 (Fig. 1). For the case of the fixed 60-day window and
 156 at 70°N and in March (spanning from 14th February to 14th April with a center on 15th March), the
 157 sampling hours distributed at 0–2, 5–11, and 21–24 LT and had a coverage of only 14 hours in
 158 2005. However, the sampling hours in 2022 distributed at 0–10 and 13–24 LT and had a coverage of
 159 22 hours. The year-to-year variations of LT distribution and coverage might induce uncertainties
 160 and biases into \bar{T}_{bk} . Thus, the YC dependent window is necessary to obtain a wide LT coverage.

161 We note that the forward drift of YC raises an issue that each YC at every year covers varying
 162 ranges of date. This aliases seasonal variation of temperature into \bar{T}_{bk} and should be removed to get
 163 a corrected mean temperature (\bar{T}_{bcrt}). The detailed procedure of the calculating \bar{T}_{bcrt} and its trend is
 164 presented in Sec. 2.1–2.3. The procedure of calculating mesopause temperature and height is
 165 presented in Sec. 2.4.

166

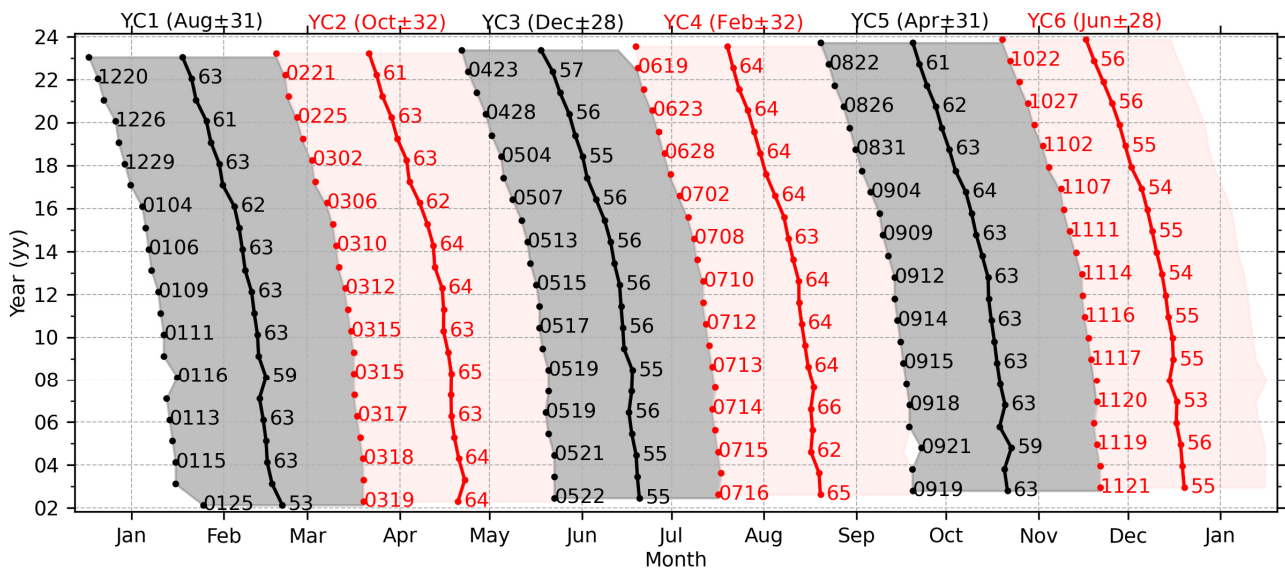


Figure 1. The temporal span of each YC from 2002 to 2023. The gray (red) region indicates the north (south) viewing maneuver. The beginning date (format of “mdd”, “mm” and “dd” mean the month and the day of month, respectively) and temporal span (unit of days) of each yaw are labeled on the right of beginning (dot) and center date (dot-line), respectively. The six YCs and their center date in 2003 and half spans and are labeled as YC1–YC6 on the top.

167

168 2.1 Removing waves from SABER temperature

169 In each YC, the background temperature is calculated at three steps. Firstly, at each latitude
170 band and pressure level, the daily zonal mean temperature (\bar{T}_d) is calculated by averaging the
171 temperature profiles at ascending and the descending nodes, respectively. This largely removes the
172 gravity waves, non-migrating tides, and long-period planetary waves. Here each latitude band has a
173 width of 10° with centers offset by 5° from 80°S to 80°N . Secondly, linear regression is performed
174 on \bar{T}_d at each node and is formulated as,

$$175 \quad \bar{T}_d = \bar{T}_{d0} + kt_{UT} + \bar{T}_{res}. \quad (1)$$

176 Here, \bar{T}_{d0} is the mean temperature in each YC. t_{UT} is the universal time with a unit of day, k
177 represents the linear variation of \bar{T}_d in each YC. After removing \bar{T}_{d0} and the linear variation (kt_{UT})
178 from \bar{T}_d , we get a residual temperature \bar{T}_{res} of each YC. Thirdly, tidal fitting is performed on \bar{T}_{res} of
179 both nodes and is formulated as,

$$180 \quad \bar{T}_{res} = \bar{T}_{bk} + \sum_{n=1}^3 a_n \cos(n\omega t_{LT} - \varphi_n). \quad (2)$$

181 Here, $\omega = 2\pi/24$ is the rotation frequency of Earth with a unit of rad/hour, t_{LT} is the local time
182 with a unit of hour, a_n and φ_n are, respectively, the amplitudes and phases of migrating diurnal
183 ($n = 1$), semidiurnal ($n = 2$) and terdiurnal ($n = 3$). Now, \bar{T}_{bk} excludes atmospheric waves and is
184 regarded as the mean temperature.

185 2.2 Removing seasonal variations from the mean temperature

186 Figure 1 shows that the center date of each YC shifts forward about one month from 2002 to
187 2023. This forward drift induces the seasonal variation of temperature into \bar{T}_{bk} . This could further
188 alias the long-term trend calculated from \bar{T}_{bk} and can be removed with the help of MSIS2.0. This is
189 because MSIS2.0 has assimilated the SABER temperature profiles during 2002–2016. The
190 climatological temperature of MSIS2.0 coincides with that of SABER within the uncertainties of \sim
191 3 K in the MLT region (Emmert et al., 2021). The detailed procedure of removing seasonal
192 variations is described below.

193 Firstly, we calculate the mean temperature of MSIS2.0. The temperature profiles (at 15
194 longitudes and 24 LTs each day) are calculated from MSIS2.0 under the conditions of lower solar
195 activity ($F_{10.7} = 50$ SFU) and geomagnetic quiet time ($ap = 4$ nT) throughout one calendar year.
196 Such that solar and geomagnetic activities do not influence the seasonal variation and trend of the
197 mean temperature. Then the daily zonal mean is performed on the temperature profiles of each day.
198 This removes tides and long-period planetary waves. The daily zonal mean temperature in each YC
199 is averaged to get the mean temperature (\bar{T}_{MSIS}^{year} , the superscript means the YC in that year). Figures
200 2(a1) and (a2) show the \bar{T}_{MSIS}^{year} at 70°N in YC3 and 70°S in YC6 during 2002–2023, respectively.

201 Secondly, we calculate the seasonal variations of each YC. The seasonal variations ($\Delta\bar{T}_{MSIS}^{year}$)

202 caused by the forward drift of each YC in different years are quantified by the difference between
 203 \bar{T}_{MSIS}^{year} of that year and the reference year (i.e., \bar{T}_{MSIS}^{2002}). For example, the difference between 2003
 204 and 2002 is calculated as $\Delta\bar{T}_{MSIS}^{2003} = \bar{T}_{MSIS}^{2003} - \bar{T}_{MSIS}^{2002}$. More specifically, since \bar{T}_{MSIS}^{year} does not include
 205 the year-to-year variations of temperature but depends on the temporal span of YC only, $\Delta\bar{T}_{MSIS}^{2003}$ in
 206 YC3 represents the seasonal variation from 20th to 19th June. Figures 3(b1) and (b2) show $\Delta\bar{T}_{MSIS}^{year}$ at
 207 70°N in YC3 and 70°S in YC6 during 2002–2023, respectively. It is evident that the forward drift of
 208 YC induces temperature variations of ± 20 K at 70°N/S from 2002 to 2023, and should be removed
 209 before we determine the long-term trends in SABER temperature.

210

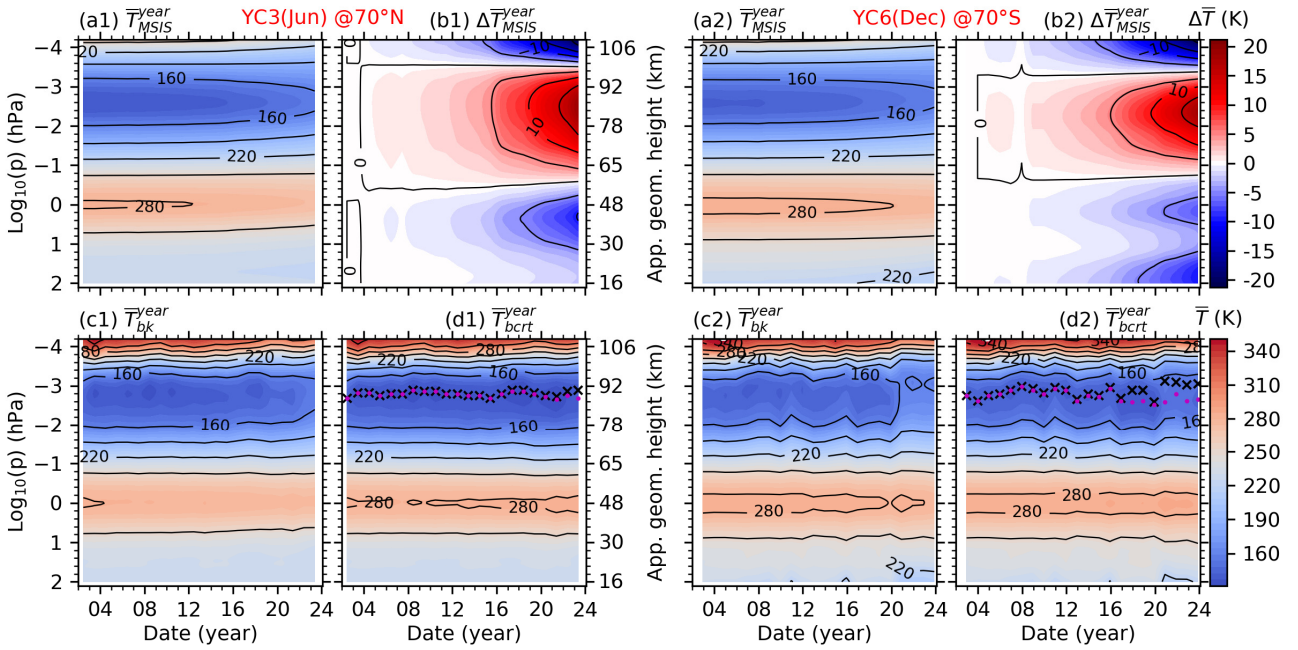


Figure 2. The date-height distributions of the mean temperature calculated from NRLMSIS 2.0 (\bar{T}_{MSIS}^{year}) and SABER (\bar{T}_{bk}^{year}) at 70°N in YC3 (left two columns) and 70°S in YC6 (right two columns). \bar{T}_{MSIS}^{year} is used as a reference to calculate the seasonal variation ($\Delta\bar{T}_{MSIS}^{year}$) caused by the forward drift of YC from 2002 to 2023. Then, the corrected mean temperature (\bar{T}_{bcr}^{year}) is calculated by removing $\Delta\bar{T}_{MSIS}^{year}$ from \bar{T}_{bk}^{year} . The mesopause heights-altitudes calculated from \bar{T}_{bk}^{year} and \bar{T}_{bcr}^{year} are plotted as black cross and red dots, respectively. The plots of \bar{T}_{MSIS}^{year} , \bar{T}_{bk}^{year} , and \bar{T}_{bcr}^{year} have the same colorbar of \bar{T} . The plot of $\Delta\bar{T}_{MSIS}^{year}$ has the colorbar of $\Delta\bar{T}$. Same scales in y-axis are used in all panels. The approximate geometric height is label on the right of the second column.

211

212 **Table 1.** The date range of each YC and its corresponding season in the reference year of 2003

YCs	YC1	YC2	YC3	YC4	YC5	YC6
Date range	20/Feb \pm 31	20/Apr \pm 32	20/Jun \pm 28	19/Aug \pm 32	13/Oct \pm 31	10/Dec \pm 28
Season	later winter	later spring	summer	early autumn	later autumn	winter

213
214
215
216
217
218
219
220
221
222
223
224
225
226
227
228
229
230
231
232
233
234
235
236
237
238
239
240
241
242
243
244
245
246

Finally, we correct the mean temperature. The corrected mean temperature (\bar{T}_{bcrt}^{year} , shown in Figs. 3d1 and d2) is obtained by removing $\Delta\bar{T}_{MSIS}^{year}$ from \bar{T}_{bk}^{year} . This removes the seasonal variation caused by the forward drift of YC from 2002 to 2023. Moreover, \bar{T}_{bcrt}^{year} retains the long-term trend of the mean temperature. We note that, after removing $\Delta\bar{T}_{MSIS}^{year}$, \bar{T}_{bcrt}^{year} covered by each YC can be represented by its center date and half span in the reference year (Tab. 1). Table 1 also lists the approximate season related to each YC.

2.3 Determining the long-term trend of the mean temperature

To calculate accurate trends in the MLT region, multi-year variations should be removed properly. The multi-year variations of temperature in the MLT region could be the solar cycle with a period of about 11 years (Beig et al., 2008; Tapping, 2013; Forbes et al., 2014; Gan et al., 2017; Qian et al., 2019), and the influences from below, such as the stratospheric quasi-biennial oscillation (QBO) with a period of about 28 months (Baldwin et al., 2001; Zhao et al., 2021) and El Niño-Southern Oscillation (ENSO) with varying cycles of around 2–7 years (Domeisen et al., 2019; Li et al., 2013, 2016; Randel et al., 2009). The solar cycle can be represented by the solar radiation flux at 10.7 cm (i.e., $F_{10.7}$ with unit of SFU= $10^{-22}\text{Wm}^{-2}\text{Hz}^{-1}$) (Tapping, 2013). ENSO is represented by multivariate ENSO index (MEI) (Domeisen et al., 2019). QBO is represented by the monthly mean zonal wind measured by radiosonde at Singapore (Baldwin et al., 2001). The multiple linear regression (MLR) method is effective to separate the long-term trend in temperature from the variations caused by solar cycle, ENSO and QBO. The MLR equation is formulated as,

$$Y(t) = c_0 + c_1t + c_2F_{10.7}(t) + c_3\text{ENSO}(t) + c_4\text{QBO}_{10}(t) + c_5\text{QBO}_{30}(t) + \varepsilon(t). \quad (3)$$

Here, Y represents the mean temperature at year t from 2002 to 2023. c_0 represents a mean state of Y . c_1 is the long-term trend of Y . c_2, c_3, c_4, c_5 represent the contributions from solar cycle, ENSO, and QBO zonal wind at 10 hPa (QBO_{10}) and 30 hPa (QBO_{30}), respectively. The terms of $F_{10.7}$, ENSO, QBO_{10} , and QBO_{30} are included in Eq. (3) for the purpose of determining long-term trend correctly but are not considered further in this work. Here we note that both the trends (linear variations) and quasi-periodical variations represent the natural variations in QBO and other predictors. These natural variations might influence the trends and variations of temperature. Thus, MLR is applied to characterize the contributions from the natural variations of predictors, and then the resulted trends of temperature exclude the trends inhibited in the predictors. This is the trend studied in this work. Otherwise, if these predictors are de-trended, their residuals are used in the MLR. The resulted trends of temperature may include the trends inhibited in predictors.

The statistical significances of the regression coefficients are measured by the student-t test

247 and the variance-covariance matrix of Eq. (3). Specifically, in Eq. (3), the sampling points are 22,
248 and the predictor variables are 6. This results in the degree of freedom of 16. Consequently, the
249 critical value is ~ 2.1 based on the student-t test at confidence level of 95% (Kutner et al., 2005).
250 This signifies that, with reference to the 95% confidence level, the magnitude of the regression
251 coefficient should be at least 2.1 times greater than the standard deviation.

252 **2.4 Determining the mesopause of each yaw cycle**

253 The mesopause temperature (\bar{T}_{msp}) is defined as the minimum of the mean temperature. The
254 pressure level where the minimum temperature occurs is defined as the mesopause ~~height-altitude~~
255 (z_{msp}). Figures 2(d1) and (d2) show the mesopause ~~altitudeheights~~ calculated from \bar{T}_{bk}^{year} (black
256 cross) and \bar{T}_{bcrt}^{year} (red dot), respectively. We see that the mesopause ~~heights-altitudes~~ calculated from
257 \bar{T}_{bk}^{year} and \bar{T}_{bcrt}^{year} are nearly identical in the first several years but exhibit discrepancies over the later
258 several years. This implies that the seasonal variation caused by the forward drift of YC affects the
259 mesopause ~~heights-altitudes~~ to some extent. Moreover, the mesopause ~~heights-altitudes~~ exhibit
260 larger variabilities in the southern summer polar region (YC6) than that in the northern summer
261 polar region (YC3). Figure 3 shows the date-latitude distributions of the mesopause temperature
262 (\bar{T}_{msp}) and ~~height-altitude~~ (z_{msp}) calculated from \bar{T}_{bcrt}^{year} . We note that z_{msp} is defined on pressure
263 level initially (Fig. 2d). To compare with previous studies, z_{msp} is interpolated onto the geometric
264 heights in Fig. 3.

265

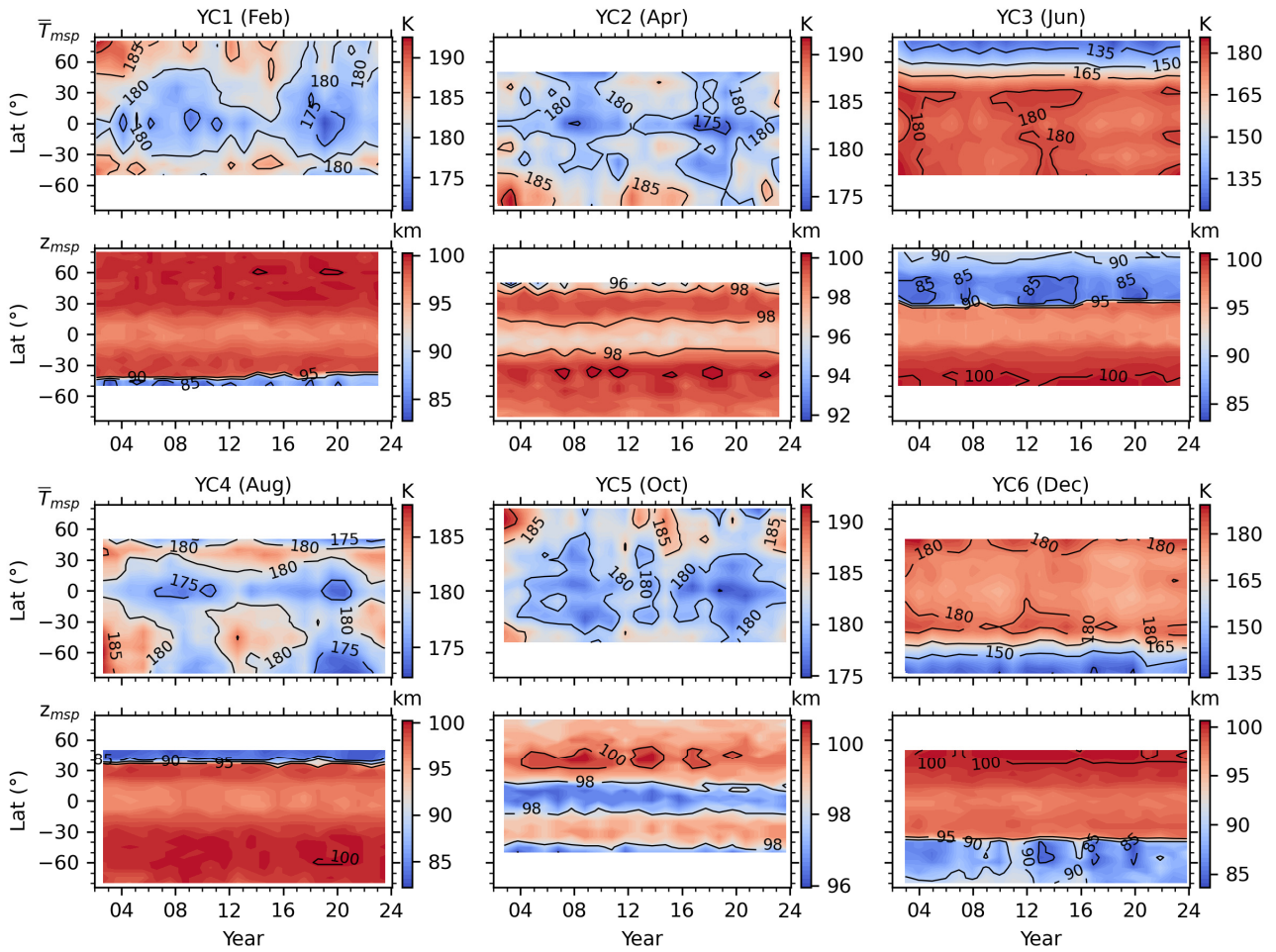


Figure 3. The date-latitude distributions of the mesopause temperature (\bar{T}_{msp} , the first and third rows) and height-altitude (z_{msp} , the second and fourth rows) calculated from \bar{T}_{bcrt}^{year} of each YC from 2002 to 2023. Here z_{msp} is interpolated from pressure level to geometric height.

266

267 Previous SABER studies often discarded high latitudes possibly due to insufficient LT
 268 coverage that induces uncertainties in the mean temperature estimation. A major advantage of
 269 binning the SABER temperature based on YC is that an accurate mean temperature can be obtained.
 270 Such that the latitude variations of \bar{T}_{msp} and z_{msp} at high latitudes can be thoroughly studied.
 271 Firstly, we focus on the YCs in northern summer and winter (i.e., YC3 and YC6) because the
 272 summer mesopause at high latitudes is more sensitive to the summer-to-winter circulation
 273 (Dunkerton, 1978; Qian et al., 2017). In YC3 (YC6), \bar{T}_{msp} and z_{msp} decrease from 50°S to 80°N
 274 (from 50°N to 80°S) in general. We note that \bar{T}_{msp} has local minima around the Equator throughout
 275 the 22 years in YC3 and YC6 and is the coldest at the highest latitudes of the summer hemisphere.
 276 z_{msp} is the lowest at 40–60°N/S throughout the 22 years. Besides the latitude variations, \bar{T}_{msp} and
 277 z_{msp} also exhibit multi-year variations. For example, \bar{T}_{msp} is colder around the Equator during the
 278 solar minima (i.e., 2007–2008, 2019–2021) in YC3 and YC6. In YC6, the lower z_{msp} at the

279 southern higher latitudes might be related to the warm phase of ENSO during 2002–2005 and
280 2016–2019.

281 In YC2 and YC5, the latitude variations of \bar{T}_{msp} and z_{msp} are almost hemispheric symmetry.
282 \bar{T}_{msp} is the coldest around the Equator and the warmest at the highest latitudes. z_{msp} is the lowest at
283 lower latitudes and the highest at the highest latitudes. In YC1, \bar{T}_{msp} and z_{msp} share the similar
284 latitude variations in winter (YC6). The difference is that \bar{T}_{msp} is warmer in YC1 than that in YC6.
285 z_{msp} is higher in YC1 than that in YC6. In YC4, \bar{T}_{msp} and z_{msp} share the similar latitude variations
286 in summer (YC3). The difference is that \bar{T}_{msp} is warmer in YC4 than that in YC3. z_{msp} is higher in
287 YC4 than that in YC3. In YC1–2 and YC4–5, multi-year variations of \bar{T}_{msp} exhibit clear solar cycle
288 dependence. At lower latitudes, \bar{T}_{msp} are colder during the solar minima (i.e., 2006–2010, 2017–
289 2021). At high latitudes, \bar{T}_{msp} are warmer during the solar maxima (i.e., 2002–2005, 2012–2014,
290 and after 2021). However, it looks like that the multi-year variations of z_{msp} are not as obvious as
291 those of \bar{T}_{msp} . These multi-year variations are considered in Eq. (3) to separate the long-term trend
292 in \bar{T}_{msp} correctly but are not considered further in this work.

293 **3 Trends of temperature in the MLT region and mesopause**

294 **3.1 Trends of temperature in the MLT region**

295 Trends of the corrected mean temperature and their significances of each YC are shown in Fig.
296 4. These trends are generally larger at high latitudes than those at lower latitudes within the six YCs.
297 Moreover, the trends show both hemispheric symmetry and asymmetry approximately in the high
298 latitude MLT region.

299 First, we describe the hemispheric symmetry in the trends. In YC1 and YC4 and above 10^{-3}
300 hPa, the cooling trends are ≥ 2 K/decade at latitudes higher than 40°N (YC1) and 40°S (YC4),
301 respectively. Around 10^{-4} hPa, the cooling trends reach their peaks of ≥ 6 K/decade. In addition,
302 there are also warming trends of ≥ 2 K/decade at latitudes higher than 30°S (YC1) and 30°N (YC4),
303 respectively. Above mesopause, there are cooling trends of ≥ 2 K/decade observed within the latitude
304 range of $20\text{--}50^\circ\text{S}$ for YC5 and $20\text{--}50^\circ\text{S}$ for YC2. Additionally, in the region just below 10^{-3} hPa,
305 there are warming trends of ≥ 2 K/decade at latitudes of $50\text{--}80^\circ\text{N}$ for YC5 and $50\text{--}80^\circ\text{S}$ for YC2. In
306 YC3 and YC6, the cooling trends of ≥ 2 K/decade shift upward from the mesopause at 80°N (YC3)
307 and 80°S (YC6) to 10^{-4} hPa at 50°S (YC3) and 50°N (YC6). There are also cooling trends of ≥ 6
308 K/decade at high latitudes of summer hemisphere. Meanwhile, the coldest trends are ≥ 10 K/decade
309 just below 10^{-4} hPa and at 80°N/S . Although the cooling trends in the MLT region have been
310 reported extensively at lower and middle latitudes (Beig et al., 2003; Laštovička, 2023), the extreme
311 cooling trends at high latitudes and above the summer mesopause have not been reported yet.

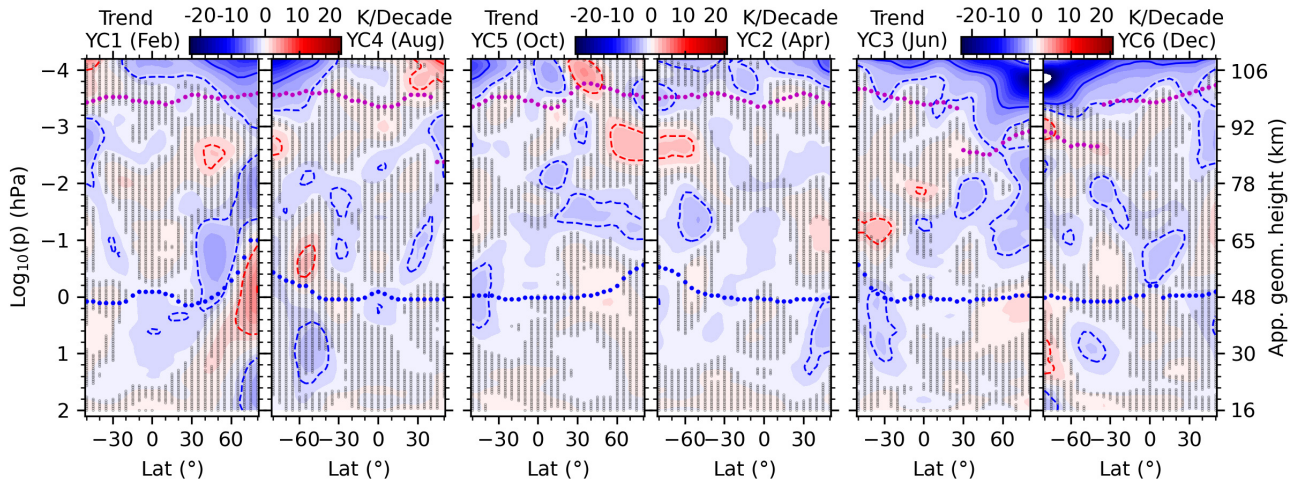


Figure 4. Trends of the corrected mean temperature in the six YCs. The solid and dashed contour lines indicate ± 6 and ± 2 K/decade, respectively. The red-purple and green-blue dots indicate the heights of the mesopause and stratopause, respectively. The regions marked by “+”shaded points indicate that trends are not significant with reference to the 95% the confidence level. The approximate geometric height is label on the last panel.

313

314 Next, we describe the hemispheric asymmetry in the trends. In YC1 and YC4, the cooling
 315 trends of ≥ 2 K/decade in YC1 extend to a wider latitude range (20°N – 80°S) than those in YC4
 316 (30°S – 80°S) above 10^{-3} hPa. The insignificant warming trends of ≥ 2 K/decade can be seen in the
 317 stratosphere at latitudes higher than 60°N in YC1 but at 45 – 60°S in YC4. In YC5 and YC2, the
 318 cooling trends of ≥ 2 K/decade can be seen around the stratopause at 30 – 50°S (YC5) but below the
 319 stratopause at 30 – 50°N (YC2). In YC3 and YC6, the significant warming trends of ≥ 2 K/decade in
 320 YC6 are stronger than those in YC3 around 0.1 hPa. In addition, the warming trends near the
 321 summer mesopause are significant in YC6 but insignificant in YC3. The simulation results in Qian
 322 et al. (2019) also demonstrated warming trends in the southern summer MLT region. Specifically,
 323 they showed significant warming trends below ~ 95 km and cooling trends above ~ 95 km at
 324 latitudes exceeding 45°S between November and February. In contrast, there were insignificant or
 325 warming trends at latitudes exceeding 45°N during June and July. Qian et al. (2019) attributed the
 326 warming trend in the summer mesosphere to the changing meridional circulation.

327 3.2 Structure and trends of the mesopause

328 Taking advantages of the continuous measurements over a long-term (22 years or equivalently
 329 two solar cycles), and YC binning at 50°S – 80°N or 80°S – 50°N , the robust mean states of the
 330 mesopause temperature (\bar{T}_{msp}) and height (z_{msp}), as well as their trends and responses of \bar{T}_{msp}
 331 to solar cycle, ENSO, QBO are quantified using MLR. Here we focus on the mean states and trends of
 332 the mesopause temperature and heightaltitude.

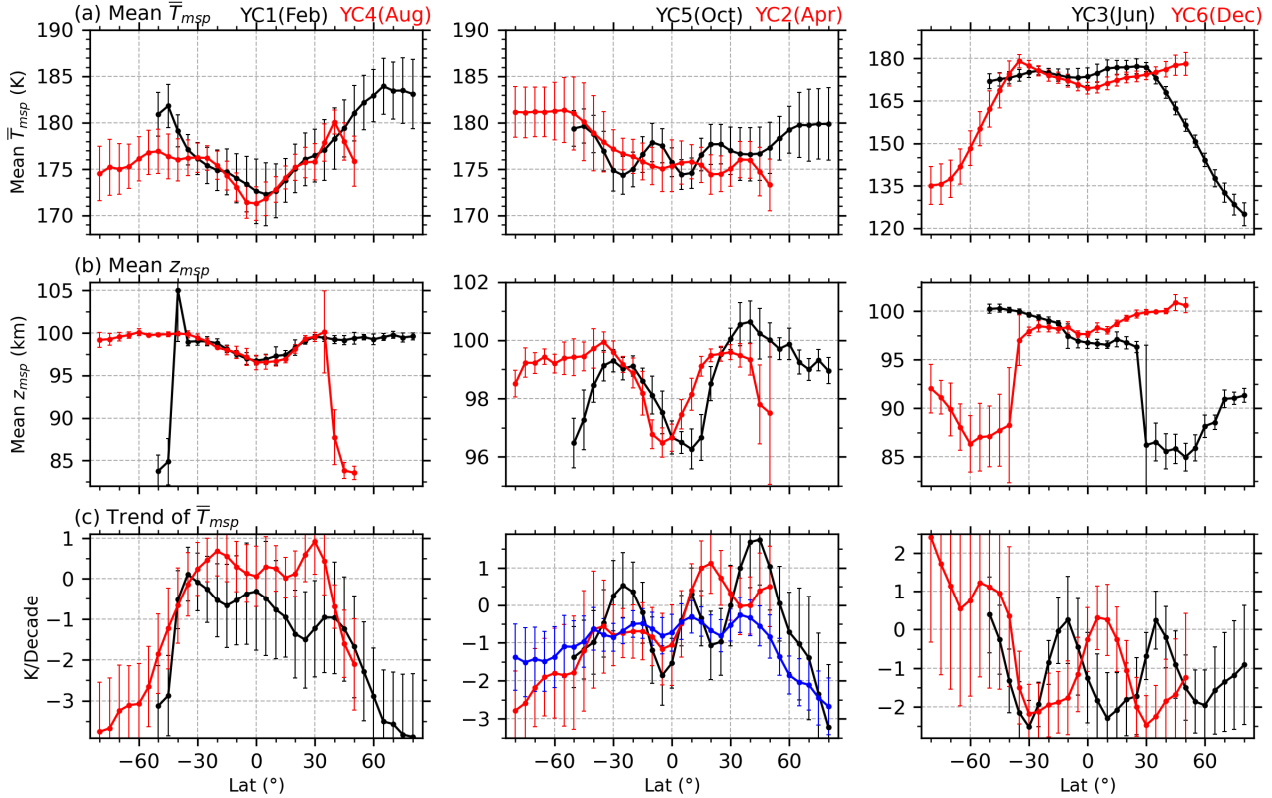


Figure 5. Latitude variations of the means of the mesopause temperature (\bar{T}_{msp} , a) and **height altitude** (z_{msp} , b) and the trends of \bar{T}_{msp} (c) of the six YCs **during 2002–2023**. The error bar of each YC indicates 2.1 times standard deviation (i.e., at 95% confidence level according to the student-t test). The all-YC mean trend of mesopause temperature is shown as a blue line in the middle panel of (c).

334

335 Figures 5(a) and 5(b) show the mean \bar{T}_{msp} and z_{msp} over 22 years of the six YCs. In YC1–2
 336 and YC4–5, the mean \bar{T}_{msp} is in the range of 172–183 K but is warmer at latitudes higher than 40°N
 337 (YC1) and 40°S (YC2) those in the counterparts of YC4 and YC5. The mean z_{msp} is mainly in the
 338 range of ~96–102 km but is higher than ~85 km at 40–50°N (YC1) and 40–50°N (YC4). In YC3,
 339 the mean \bar{T}_{msp} decreases sharply with latitudes from ~180 K at 30°N to ~125 K at 80°N. The mean
 340 z_{msp} in YC3 reaches a minimum of ~85 km at 60°N. In YC6, the mean \bar{T}_{msp} decreases sharply with
 341 latitudes from ~180 K at 35°S to ~135 K at 80°S. The mean z_{msp} in YC6 reaches a minimum of
 342 ~86 km at ~50°S. The mean \bar{T}_{msp} (z_{msp}) in the northern summer polar region is colder (lower) than
 343 that in the southern counterpart by ~5–11 K (~1 km). The hemispheric asymmetries of the summer
 344 mesopause temperature and **height altitude** coincide with Xu et al. (2007), who used the SABER
 345 temperature data during 2002–2006 and showed that the mean \bar{T}_{msp} in the summer polar region of
 346 the NH is ~5–10 K colder than its counterpart in the SH. A recent study by Wang et al. (2022), who

347 used the SABER temperature data during 2002–2020, showed that the mean \bar{T}_{msp} in the summer
348 polar region of the NH is ~ 10 K colder than its counterpart in the SH. Moreover, the transition
349 latitudes of the mean \bar{T}_{msp} (z_{msp}) from higher temperature (height) are 30°N in YC3 and 40°S in
350 YC6. This coincides well with those reported by Xu et al. (2007) and Wang et al. (2022). These
351 hemispheric asymmetries of the mean \bar{T}_{msp} and z_{msp} , and the transition latitudes could be caused
352 by the hemispheric asymmetry of solar radiation and gravity wave forcing (Xu et al., 2007).

353 Figure 5c shows that trends of \bar{T}_{msp} in YC1 and YC4 are extreme cooling (≥ 2 K/decade) at
354 latitudes higher than 55°N/S . While at $40^\circ\text{S}–40^\circ\text{N}$, trends of \bar{T}_{msp} in YC1 are cooling with
355 magnitudes of $\sim 0–2$ K/decade but are warming in YC4 with magnitudes of $\sim 0–1$ K/decade. In YC2
356 and YC5, trends of \bar{T}_{msp} are either cooling or warming, depending on the specific latitudes and
357 months being considered. At southern latitudes, trends of \bar{T}_{msp} are cooling with magnitudes of ≥ 1
358 K/decade in YC2. Trends of \bar{T}_{msp} in YC5 change sharply from 2.0 K/decade at 45°N to -3
359 K/decade at 80°N . In YC3 and YC6, trends of \bar{T}_{msp} are mainly cooling except the insignificant
360 warming trends in YC6 and at latitudes higher than 40°S . Although trends of \bar{T}_{msp} are warming at
361 some latitudes of certain YC, the all-YC mean trends of \bar{T}_{msp} (blue line in Fig. 5c) are cooling with
362 magnitudes of $0.3–1$ K/decade at $50^\circ\text{S}–50^\circ\text{N}$. At latitudes higher than 55°S , the insignificant
363 cooling trends are ≤ 1.5 K/decade. In contrast, at latitudes higher than 55°N , the significant cooling
364 trends are ≥ 1.5 K/decade.

365 4 Discussions

366 Laštovička & Jelínek (2019) pointed out that the temporal interval of data might influence the
367 long-term trend. Using the nocturnal temperature in the MLT region measured by lidars around
368 41°N and 42°N over the period of 1990–2017, She et al. (2019) demonstrated that the cooling
369 trends are $\sim 2.0–4.5$ K/decade over only one solar cycle and are $\sim 2.0–2.5$ K/decade if the data
370 length is longer than two solar cycles. Using the SABER temperature profiles during 2002–2019,
371 Zhao et al. (2020) showed that the significant trends of \bar{T}_{msp} and their responses to solar cycle can
372 be obtained at $50^\circ\text{S}–50^\circ\text{N}$ over longer than one solar cycle. Both She et al. (2019) and Zhao et al.
373 (2020) showed that the trends are relatively insensitive to the specific beginning and ending time of
374 the data as compared to the data length. Since the data length used in this study spans approximately
375 two solar cycles, the derived trends are highly reliable.

376 4.1 The reliability of trends in the MLT region at latitudes lower than 50°N/S

377 To facilitate a comparison with previously reported the annual and global-mean trends in the
378 MLT region, we present the mean trends of the corrected mean temperature at $50^\circ\text{S}–50^\circ\text{N}$ and at
379 $55–80^\circ\text{S}$ or $55–80^\circ\text{N}$ of the six YCs (Fig. 6). The mean trends at $50^\circ\text{S}–50^\circ\text{N}$ of each YC are cooling

380 with magnitudes of $\sim 0.5\text{--}1$ K/decade at $10\text{--}10^{-3}$ hPa. The exception is the warming trend of 0.2
381 K/decade around 10^{-2} hPa in YC1 and of 0.1 K/decade around 4×10^{-3} hPa in YC3. ~~At higher~~Above
382 5×10^{-3} hPa heights, the cooling trends ~~decrease~~increase sharply with ~~height~~altitude and reach to ~ 2
383 K/decade in YC5 and to ~ 3 K/decade in YC2 at 10^{-4} hPa. Compared to the situation in YC2 and
384 YC5, the cooling trends ~~decrease~~increase more sharply with ~~altitude~~height in YC3 and YC6. Their
385 magnitudes change nearly identically and are from ~ 0.5 K/decade at 2×10^{-3} hPa to ≥ 5 K/decade at
386 10^{-4} hPa. When the mean trends at $50^{\circ}\text{S}\text{--}50^{\circ}\text{N}$ across all-YC are further averaged, we obtain an
387 annual mean trend (blue line in Fig. ~~5a~~6a). The annual mean trend is cooling with magnitudes of
388 $\sim 0.5\text{--}0.8$ K/decade and vary with ~~height~~altitude slightly at $10\text{--}5\times 10^{-4}$ hPa.

389 The ~~altitude~~height variation and the magnitude of the annual mean trend are similar to the
390 previous results (Garcia et al., 2019; Mlynczak et al., 2022; Zhao et al., 2021). Figure 3 of Garcia et
391 al. (2019) revealed that the global mean ($52^{\circ}\text{S}\text{--}52^{\circ}\text{N}$) SABER temperature trends are cooling with
392 magnitudes of $\sim 0.5\text{--}0.9$ K/decade at $10\text{--}5\times 10^{-4}$ hPa during 2002–2018. These magnitudes are
393 slightly smaller than those derived from WACCM. Table 1 of Mlynczak et al. (2022) demonstrated
394 that the global mean ($55^{\circ}\text{S}\text{--}55^{\circ}\text{N}$) SABER temperature also display cooling trends with magnitudes
395 of $\sim 0.51\text{--}0.63$ K/decade at $1\text{--}10^{-3}$ hPa. Similarly, Fig. 4 of Zhao et al. (2021) revealed that the
396 global mean ($50^{\circ}\text{S}\text{--}50^{\circ}\text{N}$) SABER temperature trends are cooling with magnitudes of $\sim 0.5\text{--}0.9$
397 K/decade at 30–105 km. At 10^{-4} hPa, the extreme cooling trend of 2.6 K/decade in Table 1 of
398 Mlynczak et al. (2022) is slightly smaller than the ~~5–2.8~~ K/decade derived here but within 2 times of
399 the standard deviation (blue line in Fig. 6a). Further examining the trends across the six YCs (Figs.
400 4 and 6a), it becomes evident that the extreme cooling trend is mainly attributed to the middle
401 latitudes of summer hemisphere (i.e., YC3 and YC6) and partially from other months. As suggested
402 by Mlynczak et al. (2022), the extreme cooling trend at 10^{-4} hPa is due to a decrease in solar
403 irradiance that is not captured by the $F_{10.7}$ index.

404 These detailed comparisons showed that the trends at pressure levels reported by Garcia et al.
405 (2019) and Mlynczak et al. (2022) support the ~~height~~altitude variations and magnitudes of the trends
406 derived here directly. Although the trends reported by Zhao et al. (2021) are in geometric height,
407 their ~~height~~altitude variations and magnitudes agree with the trends derived here, too. Thus, the
408 method of binning SABER samplings based on YC leads a reliable global mean trends at $50^{\circ}\text{S}\text{--}$
409 50°N . Moreover, this method provides an opportunity to study the trends at latitudes higher than
410 ~~55~~50 $^{\circ}\text{N/S}$ in certain months.

411

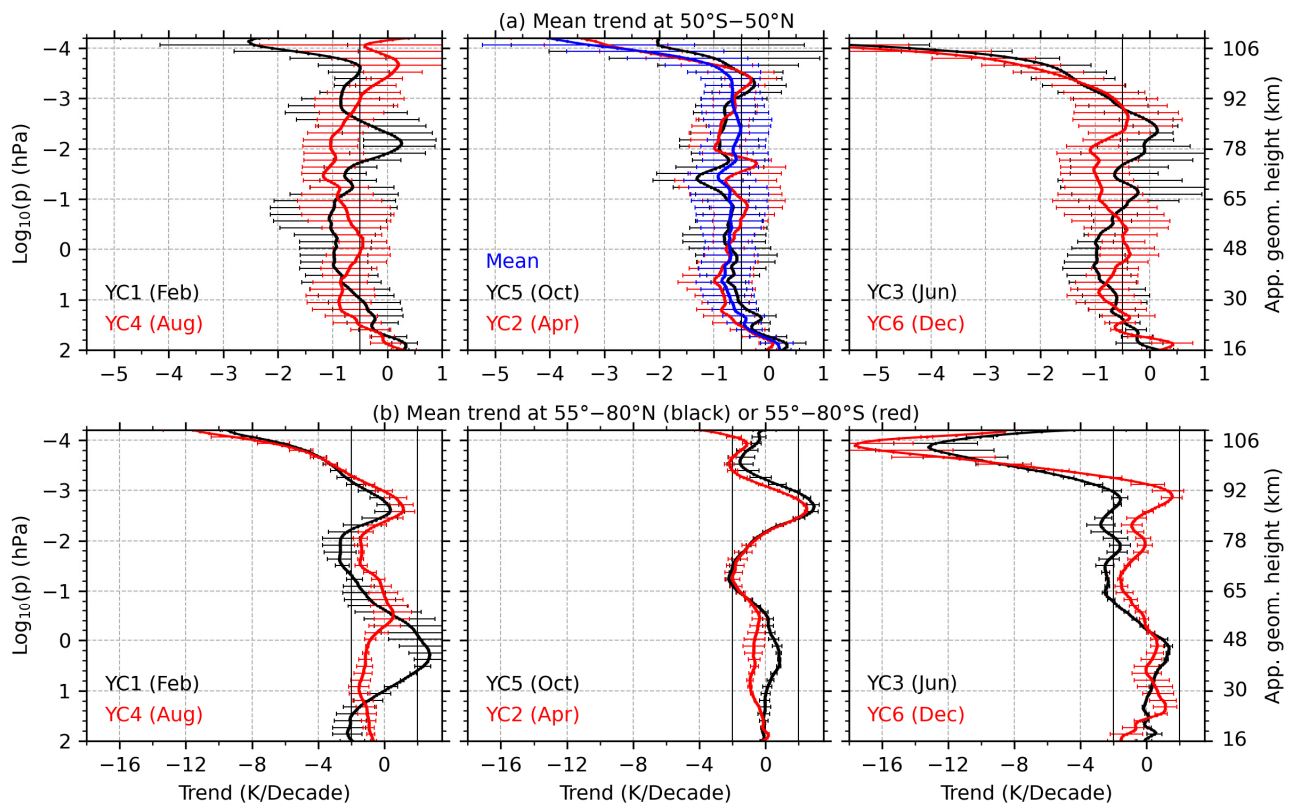


Figure 6. Mean trends of the corrected mean temperature at 50°S–50°N (a) and at 55–80°S (red line in b) or 55–80°N (black line in b) of the six YCs. The annual mean trend is calculated by averaging the trends of the six YCs at 50°S–50°N and is shown a blue line in the middle panel of (a). The error bars indicate standard errors of the averaged data.

412

413 4.2 The reliability of trends in the MLT region at latitudes higher than 50°N/S

414

415 At latitudes higher than 55°N/S, the height-altitude variations of the mean trends of the six
 416 YCs (Fig. 6b) are seasonal symmetric approximately above 1 hPa. The magnitudes of trends are
 417 mainly in the range of -2–2 K/decade below the height of 10^{-3} hPa. An interesting feature is the
 418 warming trends of 1–2.5 K/decade at 10^{-2} – 10^{-3} hPa in April, August, October, and December. The
 419 altitudes of peaks of the warming trends vary from 4×10^{-3} hPa to 10^{-3} hPa in different months.
 420 Focusing on the latitude band of 64–70°N in June and 64–70°S in December, Bailey et al. (2021)
 421 merged the temperature data from HALO and SABER (total length of 29 years) and HALOE and
 422 SOFIE (total length of 22 years). Their analysis revealed warming trends of 1–2 K/decade near
 423 5×10^{-3} hPa (~ 85 km) at 64–70°N in June and 64–70°S in December, as illustrated in Fig. 7 of their
 424 paper. The results simulated by WACCM-X showed significant warming trends at ~ 80 –95 km at
 425 latitudes higher than 45°S from November to February and close to zero or warming trends at
 426 latitudes higher than 45°N from June to July (Qian et al., 2019). The warming trends in December
 427 derived here coincides with those reported by Bailey et al. (2021) and Qian et al. (2019). The weak

428 warming trend at 2×10^{-3} hPa in June coincides with those in Qian et al. (2021) but is much smaller
429 than the 1–2 K/decade reported by Bailey et al. (2021). In April and October, the warming trends
430 are hemispheric symmetric at 10^{-2} – 10^{-3} hPa and reach peak of ≥ 2 K/decade at 3×10^{-3} hPa. Above
431 10^{-3} hPa, the trends transit from warming to cooling.

432 We can see the extreme cooling trends of ≥ 6 K/decade above $\sim 10^{-3}$ hPa and in YC3 and YC6
433 also in YC1 and YC4 but around 10^{-4} hPa. These cooling trends are comparable with the global
434 average mesosphere temperature of 6.8–8.4 K/decade derived by Mlynczak et al. (2022) after
435 doubling of CO₂ at Earth’s surface. However, it takes decades to doubled CO₂. Thus, a purely
436 radiative effect due to the increasing CO₂ cannot support the extrem cooling trends derived here.
437 Mlynczak et al. (2022) proposed that the F10.7 is not a suitable proxy to indicate effects of the solar
438 radiations on the lower thermosphere. But the solar irradiance in the Schumann–Runge band (175–
439 200 nm) might be responsible for the colder trend. Even so, the extreme cooling trends of ~ 10
440 K/decade are still larger than those reported by Mlynczak et al. (2022). Other possible reasons for
441 the extreme cooling trends in the high latitude MLT region can be attributed to: (1) the dynamical
442 feedback in the polar MLT region; (2) the uncertainties of the SABER temperature measurements.

443 Besides the purely radiative effect on the cooling trends in the MLT region (i.e., Garcia et al.,
444 2019, Mlynczak et al., 2022), the dynamical feedback might be another cause of the cooling trends.
445 Based on the simplified Eulerian mean (TEM) thermodynamic equation, the temperature change
446 (ΔT) caused by dynamics can be written as (Eq. 3 and 4 of Yu et al. (2023)),

$$447 \quad \Delta T = -\alpha^{-1} \left(w^* S + v^* \frac{\partial \bar{T}}{a \partial \varphi} \right). \quad (4)$$

448 Here, α is the Newtonian cooling coefficient. w^* and v^* are the residual vertical and meridional
449 velocity, respectively. S and \bar{T} are the static stability and zonal mean temperature, respectively. a
450 and φ are the Earth’s radius and latitude, respectively. From Eq. (4), we propose that ~~T~~the extreme
451 cooling trends at high latitudes of the summer hemispheres (YC3 and YC6) might be resulted from
452 the changing summer-to-winter circulation and gravity wave forcing in the MLT region. The
453 circulation is upwelling (positive w^*) in the summer hemisphere and causes a cold summer
454 mesosphere through adiabatic cooling. Conversely, in the winter hemisphere, the circulation is
455 downwelling (negative w^*), leading to a warm winter mesosphere through adiabatic warming
456 (Garcia and Solomon, 1985). A necessary condition for the extreme cooling trends at summer high
457 latitudes is the stronger upwelling and thus the increasing gravity wave body force in the summer
458 hemispheres. Previous studies showed that the potential energy of gravity waves (GWPE) in the
459 MLT region exhibited significant positive trends at southern high latitudes in January and at
460 northern high latitudes in July (Fig. 5 of Liu et al., 2017). The positive trends of GWPE might
461 enhance the strength of upwelling and thus result in the extreme cooling trends at high latitudes of

462 summer hemispheres. It should be noted that the dynamical feedback in the MLT region is only
463 analyzed qualitatively, the quantitative analysis should be performed through model simulations.
464 Such that one can elucidate the physics behind the strong cooling trend in the polar MLT region.

465 The main causes of the operational SABER temperature systematic uncertainties are the lack
466 of accurate knowledge of atomic oxygen and carbon dioxide during the retrieval process. The
467 atomic oxygen provided to the operational SABER temperature retrieval algorithm is from
468 NRLMSISE-00 (Picone et al., 2002). Below 100 km, no atmospheric observations of atomic
469 oxygen are incorporated. Thus, the uncertainty of atomic oxygen influences the uncertainties of
470 temperature from ~75 km to 110 km, in particular, above 100 km. The carbon dioxide provided to
471 the operational SABER temperature retrieval algorithm is the monthly average value from WACCM
472 model (Dawkins et al., 2018; Picone et al., 2002). Thus, there is no local time variation in carbon
473 dioxide used in the operational SABER temperature algorithm. This will induce uncertainties of
474 SABER temperature and thus the uncertainties of trends above 75 km.

475 These uncertainties in temperature may not be constant or stable in time or in space. To explore
476 the impacts of the uncertainties in SABER temperature on the derived trends, we performed Monte
477 Carlo simulations by assuming the uncertainties in SABER temperature following a uniform
478 distribution in the range of $\pm 25\text{K}$. In each time of Monte Carlo simulation, in each YC and at each
479 pressure level and within a latitude band of 10° , the SABER samplings (more than 5000 data) are
480 added by random numbers following the uniform distribution in the range of $\pm 25\text{K}$. Then same
481 procedure described in Sec. 2.1–2.3 was repeated to derive trends. The Monte Carlo simulations
482 were performed 5000 times (see Appendix). The main result is that the uncertainties of $\pm 25\text{K}$ in
483 SABER samplings would induce a mean temperature variation of $\sim 1\text{--}3\text{ K}$ and a false trend of $\sim 0.5\text{--}$
484 1.2 K/decade at high latitudes. This is mainly because the mean temperature is calculated from
485 more than 5000 data in each YC within a latitude band of 10° , which reduces the standard deviation
486 by a factor of $\sim 1/250$ based on central limit theory. It must be noted that the actual distributions of
487 the uncertainties in SABER samplings caused by atomic oxygen and carbon dioxide are unknown.
488 The Monte Carlo simulation only provides a reference result by assuming the uncertainties
489 following uniform distributions. This may not be valid for the case of SABER temperature
490 systematic errors. So may not be valid. We only include it in the Appendix.

491 **4.24.3 The reliability of the mesopause trends**

492 The trends of \bar{T}_{msp} derived in this study are significant and mainly negative at $50^\circ\text{S}\text{--}50^\circ\text{N}$
493 across most YCs. The averaged trend of \bar{T}_{msp} of the six YCs is $-0.64\pm 0.22\text{ K/decade}$ over $50^\circ\text{S}\text{--}$
494 50°N . When the average is performed over $80^\circ\text{S}\text{--}80^\circ\text{N}$, the trend of \bar{T}_{msp} of the six YCs is $-$
495 $1.03\pm 0.40\text{ K/decade}$. The cooling trend of \bar{T}_{msp} derived here coincides also with the -0.5 ± 0.21

496 K/decade in the mesosphere (Garcia et al., 2019) within only 50°S–50°N. Compared to the trend
497 derived from sodium lidar observations during nighttime only around 40°N, the trends of \bar{T}_{msp} from
498 SABER are about -0.1, 0.0, -0.2, -0.8, 0.6, -1.9 K/decade in the six YCs and have annual mean of -
499 0.4 K/decade. This is less than the significant cooling trend of 2.3–2.5 K/decade during 1990–2018
500 but is consistent with the insignificant cooling trend of 0.2–1 K/decade during 2000–2018 (Yuan et
501 al., 2019). The comparisons of \bar{T}_{msp} between our results and those from satellite, ground-based
502 observations exhibit general consistencies in the sense of annual mean or global-mean.

503 A notable feature is the warming trends of \bar{T}_{msp} with magnitudes of 0–2 K/decade at latitudes
504 higher than 40°S in YC6. This warming trend is insignificant under 95% confidence level. If we
505 change the temporal interval from 2002–2023 to 2002–2019, the trends of \bar{T}_{msp} are cooling with
506 magnitudes of 1–2 K/decade. Here we note that the year 2020 is just after the time when the
507 SABER temperature data was revised (version 2.08, since 15 December 2019) (Mlynczak et al.,
508 2023). In this work, we use the SABER temperature data of versions 2.07 (before 15 December
509 2019) and 2.08 (after 15 December 2019). According to Mlynczak et al. (2023), the new released
510 data are free from the algorithm instability. On the other hand, there is no significant difference in
511 the counterpart of YC3. A recent study by Yu et al. (2023) showed that the Hunga Tonga Hunga-
512 Ha'apai (HTHH) volcanic eruption on 15 January 2022 induced temperature anomalies of ± 10 K
513 globally in the stratosphere and mesosphere in August. The anomalies disappeared after September
514 2022. This indicates that the volcanic eruption may influence the mesosphere temperature through
515 circulations and waves. From the mesopause temperature of YC6 shown in Fig. 3, we see that the
516 warmer mesopause occurred after 2020 before the HTHH volcanic eruption. Thus, the largest
517 difference in YC6 may not be caused by the algorithm instability or the HTHH volcanic eruption but
518 a realistic result. As shown in Figs. 2(d) and 5(b) and reported by Wang et al. (2022), the annual
519 variability of z_{msp} is ~ 5 km at the southern high latitudes (YC6) but is relative stable at the northern
520 high latitudes (YC3). The large annual variability of z_{msp} induces a large variability of \bar{T}_{msp}
521 (indicated by large standard deviations in the right panel of Fig. 5b). This in turn contributes to the
522 large variability of the trends of \bar{T}_{msp} at southern high latitudes.

523 **5 Summary**

524 Using the temperature profiles measured by the SABER instrument throughout the period of
525 2002–2023 (about two solar cycles) and binning them based on yaw cycles (YCs), we get
526 continuous data with good LT coverage within the range of 50°S–80°N or 80°S–50°N. Then we can
527 obtain an accurate mean temperature ~~excluding~~ atmospheric waves. The temporal span of
528 each YC drifted forward about one month from 2002 to 2023, aliasing the seasonal change in
529 temperature into long-term trends. This season change is removed by using the climatological

530 temperature of MSISE2.0. The remaining temperature is regarded as the corrected mean
531 temperature (\bar{T}_{bcrt}^{year}) of each YC. Then the mesopause temperature (\bar{T}_{msp}) and height (\bar{z}_{msp}) are
532 calculated from \bar{T}_{bcrt}^{year} . Such that the trends of the mean temperature and the mesopause structure
533 can be studied in each YC at high latitudes using MLR. The main results are summarized as below:

534 The cooling trends are significant in the MLT region and coincide well with previous results at
535 50°S–50°N. At latitudes higher than 55°N, the new findings are that the cooling trends have
536 magnitudes of ≥ 2 K/decade at northern high latitudes in February, April, and June and at southern
537 high latitudes in August, October, and December. There are also extreme cooling trends of ≥ 6
538 K/decade in the lower thermosphere at the northern highest latitude in February and June and at the
539 southern highest latitudes in August and December. Both the cooling and extreme cooling trends are
540 hemispheric and seasonal symmetric.

541 Besides the general cooling trends, there are also warming trends of 1–2.5 K/decade at 10^{-2} – 10^{-3}
542 hPa and at latitudes higher than 55°N in October and December and at latitudes higher than 55°S
543 in April and August. The peaks of the warming trends vary from 4×10^{-3} hPa to 10^{-3} hPa in different
544 months. The warming trend in December coincides with previous observational and simulation
545 results.

546 The mean $\bar{T}_{msp}(z_{msp})$ in the northern summer polar region is colder (lower) than that in the
547 southern counterpart by a value of ~ 5 – 11 K (~ 1 km) over the past 22 years. Although the trends of
548 \bar{T}_{msp} are highly dependent on latitudes and months, they are negative at most latitudes and have
549 larger magnitudes at higher latitudes. The trends of \bar{T}_{msp} at the southern high latitudes in December
550 are highly dependent on the data length. The trends of \bar{T}_{msp} change from warming of 0–2 K/decade
551 during 2002–2023 to cooling of 1–2 K/decade during 2002–2019. The significant dependence of the
552 trends of \bar{T}_{msp} on the data length might be caused by the large annual variability of z_{msp} at the
553 southern high latitudes in December.

554 The trends of the mean temperature in the MLT region and mesopause are revealed from
555 continuous observations of the SABER instrument over the past 22 years. The data length is long
556 enough to determine reliable trends. Our results provide an observational proof that the extreme
557 cooling trends at high latitudes are more sensitive to the changing dynamics associated with climate
558 change and should be paid more attentions in future observational and model studies.

559 Appendix

560 Around 10^{-4} hPa, the uncertainties of SABER temperature measurements are around 25 K at
561 mid-latitudes and are likely higher at high latitudes. These uncertainties are mainly attributed to the
562 uncertainties of atomic oxygen and carbon dioxide, which were used in the operational SABER
563 temperature retrieval algorithm. Moreover, these uncertainties in temperature may not be constant

564 or stable in time or in space. To explore the impacts of the uncertainties in SABER temperature on
565 the derived trends, we performed Monte Carlo simulations by assuming the uncertainties in SABER
566 temperature following a uniform distribution in the range of $\pm 25\text{K}$. In each time of Monte Carlo
567 simulation, in each YC and at each pressure level and within a latitude band of 10° , the SABER
568 samplings (more than 5000 data) are added by random numbers following the uniform distribution
569 in the range of $\pm 25\text{K}$. Then same procedure described in Sec. 2.1–2.3 was repeated to derive trends.
570 The Monte Carlo simulations were performed 5000 times to get convincing results.

571 Since the cooling trends are very large in YC3 and at 75°N , especially around the pressure
572 levels of around 10^{-4} hPa, we show in Figure A the impact of the random uncertainties of SABER
573 temperature on the derived trends in YC3 and at 75°N . The uncertainties of $\pm 25\text{K}$ in SABER
574 samplings induce the mean temperature (\bar{T}_{bk}^{2002}) varying in the range of ± 2 K (Fig. Aa1) with
575 standard deviation of 0.5 K (Fig. Aa2) at 10^{-4} hPa. This in turn induces the trends varying in the
576 range of ± 0.6 K/decade (Fig. Ab1) with standard deviation of 0.15 K/decade (Fig. Ab2) at 10^{-4} hPa.
577 The altitude profile of \bar{T}_{bk}^{2002} by assuming a zero uncertainty is similar to that calculated by
578 assuming the random uncertainties of $\pm 25\text{K}$ (Fig. Ac1). The differences of the maximum and
579 minimum of \bar{T}_{bk}^{2002} among the 5000 times of Monte Carlo simulations are $\sim 1\text{--}2$ K below 5×10^{-4} hPa
580 and are ≥ 3 K around 10^{-4} hPa (Fig. Ac2). The altitude profile of trend by assuming a zero
581 uncertainty is similar to that calculated by assuming the random uncertainties of $\pm 25\text{K}$ (Fig. Ad1).
582 The differences of the maximum and minimum of trend among the 5000 times of Monte Carlo
583 simulations are ~ 0.5 K/decade below 10^{-3} hPa and are $\sim 0.5\text{--}1.2$ K/decade around 10^{-4} hPa (Fig.
584 Ad2). This example illustrates that the uncertainties of $\pm 25\text{K}$ in SABER samplings would induce a
585 mean temperature variation of $\sim 1\text{--}3$ K and a false trend of $\sim 0.5\text{--}1.2$ K/decade at high latitudes.

586

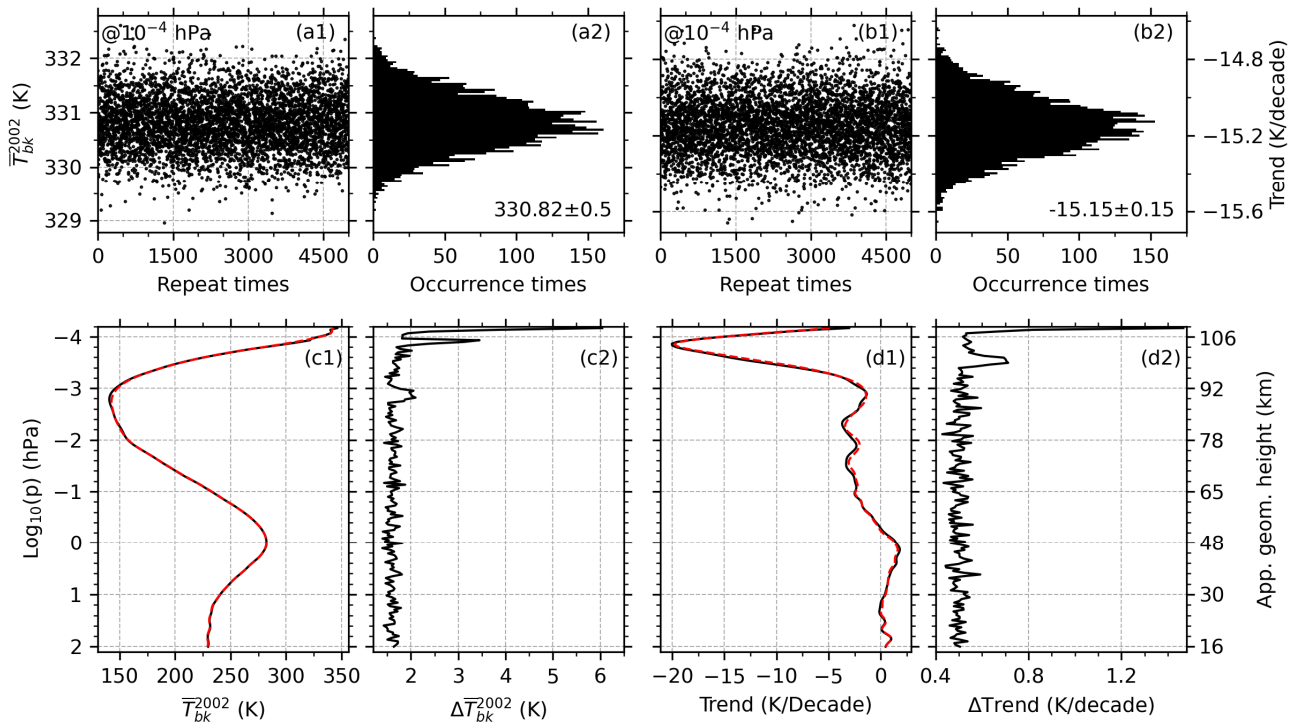


Figure A. The impacts of random uncertainties of $\pm 25\text{K}$ in SABER temperature on the derived trends in YC3 and at 75°N during 5000 times of Monte Carlo simulation. (a1) and (a2): the mean temperature calculated from SABER sampling (\bar{T}_{bk}^{2002}) and its histogram at 10^{-4} hPa; (b1) and (b2): the trend and its histogram at 10^{-4} hPa; (c1) and (d1): the altitude profiles of \bar{T}_{bk}^{2002} by assuming zero uncertainty (black) and random uncertainties of $\pm 25\text{K}$ (dashed-black); (c2) and (d2) altitude profile of the difference between the maximum and minimum of \bar{T}_{bk}^{2002} and trend.

587

588 Another Monte Carlo simulation is performed to test the impacts of the uncertainties of $\pm 25\text{K}$
 589 on the mean temperature (180 K) by changing the sampling points. During 5000 times of
 590 simulations (not shown here), the mean temperature and its standard deviation are 179.956 ± 4.5 K if
 591 there are 10 samplings; the mean temperature and its standard deviation are 179.977 ± 1.43 K if there
 592 are 100 samplings; the mean temperature and its standard deviation are 179.997 ± 0.20 K if there are
 593 5000 samplings. This indicates that the increasing samplings can reduce the measurement
 594 uncertainties efficiently. Although the uncertainties of SABER samplings are as large as $\pm 25\text{K}$ at
 595 high latitudes, its impact on the trends are insignificant in the highly averaged results. This is mainly
 596 because mean temperature is calculated from more than 5000 data in each YC within a latitude band
 597 of 10° , which reduces the standard deviation by a factor of $\sim 1/250$ based on central limit theory. It
 598 must be noted that the actual distributions of the uncertainties in SABER samplings are unknown.
 599 The Monte Carlo simulation only provides a reference result by assuming the uncertainties
 600 following uniform distribution. This may not be valid for the case of SABER temperature
 601 systematic errors.

602

603 **Author contributions**

604 XL analyzed the data and prepared the paper with assistance from all co-authors. JX and JY
605 design the study. All authors reviewed and commented on the paper.

606 **Data Availability Statement**

607 All SABER data can be accessed from Space Physics Data Facility, Goddard Space Flight
608 Center (<https://spdf.gsfc.nasa.gov/pub/data/timed/saber/> (last access: January 2024; Mlynczak et al.,
609 2023). The $F_{10.7}$ data were obtained from <https://spdf.gsfc.nasa.gov/pub/data/omni/> (last access:
610 January 2024; Tapping, 2013). The QBO data were obtained from [https://acd-
611 ext.gsfc.nasa.gov/Data_services/met/qbo/](https://acd-ext.gsfc.nasa.gov/Data_services/met/qbo/) (last access: January 2024; Baldwin et al., 2001). The
612 ENSO data were obtained from <https://www.psl.noaa.gov/enso/mei/> (last access: January 2024;
613 Zhang et al., 2019; Wolter and Timlin, 2011)

614 **Competing interests**

615 The authors declare that they have no conflict of interest.

616 **Acknowledgments**

617 This work was supported by the National Natural Science Foundation of China (41874182,
618 42174196), the Project of Stable Support for Youth Team in Basic Research Field, CAS (YSBR-
619 018), the Informatization Plan of Chinese Academy of Sciences (CAS-WX2021PY-0101), and the
620 Open Research Project of Large Research Infrastructures of CAS "Study on the interaction between
621 low/mid-latitude atmosphere and ionosphere based on the Chinese Meridian Project". This work
622 was also supported in part by the Specialized Research Fund and the Open Research Program of the
623 State Key Laboratory of Space Weather. [We are very grateful for the helpful comments by Jan
624 Laštovička, Martin Mlynczak, and one anonymous reviewer.](#)

625 **References**

- 626 Bailey, S. M., Thurairajah, B., Hervig, M. E., Siskind, D. E., Russell, J. M., and Gordley, L. L.: Trends in the polar
627 summer mesosphere temperature and pressure altitude from satellite observations, *J. Atmos. Solar-Terrestrial*
628 *Phys.*, 220, 105650, <https://doi.org/10.1016/j.jastp.2021.105650>, 2021.
- 629 Baldwin, M. P., Gray, L. J., Dunkerton, T. J., Hamilton, K., Haynes, P. H., Randel, W. J., Holton, J. R., Alexander, M.
630 J., Hirota, I., Horinouchi, T., Jones, D. B. A., Kinnnersley, J. S., Marquardt, C., Sato, K., and Takahashi, M.: The
631 quasi-biennial oscillation, *Rev. Geophys.*, 39, 179–229, <https://doi.org/10.1029/1999RG000073>, 2001.
- 632 Beig, G., Keckhut, P., Lowe, R. P., Roble, R. G., Mlynczak, M. G., Scheer, J., Fomichev, V. I., Offermann, D., French,
633 W. J. R., Shepherd, M. G., Semenov, A. I., Remsberg, E. E., She, C. Y., Lübken, F. J., Bremer, J., Clemesha, B. R.,
634 Stegman, J., Sigernes, F., and Fadnavis, S.: Review of mesospheric temperature trends, *Rev. Geophys.*, 41,
635 <https://doi.org/10.1029/2002RG000121>, 2003.

636 Beig, G., Scheer, J., Mlynczak, M. G., and Keckhut, P.: Overview of the temperature response in the mesosphere and
637 lower thermosphere to solar activity, *Rev. Geophys.*, 46, <https://doi.org/10.1029/2007RG000236>, 2008.

638 Dalin, P., Perminov, V., Pertsev, N., and Romejko, V.: Updated Long-Term Trends in Mesopause Temperature,
639 Airglow Emissions, and Noctilucent Clouds, *J. Geophys. Res. Atmos.*, 125, 1–19,
640 <https://doi.org/10.1029/2019JD030814>, 2020.

641 Das, U.: Spatial variability in long-term temperature trends in the middle atmosphere from SABER/TIMED
642 observations, *Adv. Sp. Res.*, 68, 2890–2903, <https://doi.org/10.1016/j.asr.2021.05.014>, 2021.

643 Dawkins, E. C. M., Feofilov, A., Rezac, L., Kutepov, A. A., Janches, D., Höffner, J., Chu, X., Lu, X., Mlynczak, M. G.,
644 and Russell, J.: Validation of SABER v2.0 operational temperature data with ground-based lidars in the
645 mesosphere-lower thermosphere region (75–105 km), *J. Geophys. Res. Atmos.*, 123, 9916–9934,
646 <https://doi.org/10.1029/2018JD028742>, 2018.

647 Domeisen, D. I. V., Garfinkel, C. I., and Butler, A. H.: The teleconnection of El Niño Southern Oscillation to the
648 stratosphere, *Rev. Geophys.*, 57, 5–47, <https://doi.org/10.1029/2018RG000596>, 2019.

649 Dunkerton, T.: On the Mean Meridional Mass Motions of the Stratosphere and Mesosphere, *J. Atmos. Sci.*, 35, 2325–
650 2333, [https://doi.org/10.1175/1520-0469\(1978\)035<2325:OTMMMM>2.0.CO;2](https://doi.org/10.1175/1520-0469(1978)035<2325:OTMMMM>2.0.CO;2), 1978.

651 Emmert, J. T., Drob, D. P., Picone, J. M., Siskind, D. E., Jones, M., Mlynczak, M. G., Bernath, P. F., Chu, X.,
652 Doornbos, E., Funke, B., Goncharenko, L. P., Hervig, M. E., Schwartz, M. J., Sheese, P. E., Vargas, F., Williams,
653 B. P., and Yuan, T.: NRLMSIS 2.0: A Whole-Atmosphere Empirical Model of Temperature and Neutral Species
654 Densities, *Earth Sp. Sci.*, 8, <https://doi.org/10.1029/2020EA001321>, 2021.

655 Forbes, J. M., Zhang, X., and Marsh, D. R.: Solar cycle dependence of middle atmosphere temperatures, *J. Geophys.*
656 *Res. Atmos.*, 119, 9615–9625, <https://doi.org/10.1002/2014JD021484>, 2014.

657 French, W. J. R., Mulligan, F. J., and Klekociuk, A. R.: Analysis of 24 years of mesopause region OH rotational
658 temperature observations at Davis, Antarctica – Part 1: long-term trends, *Atmos. Chem. Phys.*, 20, 6379–6394,
659 <https://doi.org/10.5194/acp-20-6379-2020>, 2020.

660 Gan, Q., Du, J., Fomichev, V. I., Ward, W. E., Beagley, S. R., Zhang, S., and Yue, J.: Temperature responses to the 11
661 year solar cycle in the mesosphere from the 31 year (1979–2010) extended Canadian Middle Atmosphere Model
662 simulations and a comparison with the 14 year (2002–2015) TIMED/SABER observations, *J. Geophys. Res. Sp.*
663 *Phys.*, 122, 4801–4818, <https://doi.org/10.1002/2016JA023564>, 2017.

664 Garcia, R. R. and Solomon, S.: The effect of breaking gravity waves on the dynamics and chemical composition of the
665 mesosphere and lower thermosphere., *J. Geophys. Res.*, 90, 3850–3868, <https://doi.org/10.1029/JD090iD02p03850>,
666 1985.

667 Garcia, R. R., Yue, J., and Russell, J. M.: Middle atmosphere temperature trends in the twentieth and twenty-First
668 centuries simulated with the Whole Atmosphere Community Climate Model (WACCM), *J. Geophys. Res. Sp.*
669 *Phys.*, 124, 7984–7993, <https://doi.org/10.1029/2019JA026909>, 2019.

670 Kutner, M., Neter, C. N. J., and Li, W.: *Applied Linear Statistical Models*, 5th ed., McGraw-Hill Irwin, Boston, 1396
671 pp., 2005.

672 Laštovička, J.: Global pattern of trends in the upper atmosphere and ionosphere: Recent progress, *J. Atmos. Solar-*
673 *Terrestrial Phys.*, 71, 1514–1528, <https://doi.org/10.1016/j.jastp.2009.01.010>, 2009.

674 Laštovička, J.: Progress in investigating long-term trends in the mesosphere, thermosphere, and ionosphere, *Atmos.*
675 *Chem. Phys.*, 23, 5783–5800, <https://doi.org/10.5194/acp-23-5783-2023>, 2023.

676 Laštovička, J. and Jelínek, Š.: Problems in calculating long-term trends in the upper atmosphere, *J. Atmos. Solar-*
677 *Terrestrial Phys.*, 189, 80–86, <https://doi.org/10.1016/j.jastp.2019.04.011>, 2019.

678 Laštovička, J., Akmaev, R. A., Beig, G., Bremer, J., and Emmert, J. T.: Global Change in the Upper Atmosphere,
679 *Science (80-.)*, 314, 1253–1254, <https://doi.org/10.1126/science.1135134>, 2006.

680 Li, T., Calvo, N., Yue, J., Dou, X., Russell, J. M., Mlynczak, M. G., She, C. Y., and Xue, X.: Influence of El Niño-
681 Southern oscillation in the mesosphere, *Geophys. Res. Lett.*, 40, 3292–3296, <https://doi.org/10.1002/grl.50598>,

682 2013.

683 Li, T., Calvo, N., Yue, J., Russell, J. M., Smith, A. K., Mlynczak, M. G., Chandran, A., Dou, X., and Liu, A. Z.:
684 Southern Hemisphere summer mesopause responses to El Niño-Southern Oscillation, *J. Clim.*, 29, 6319–6328,
685 <https://doi.org/10.1175/JCLI-D-15-0816.1>, 2016.

686 Li, T., Yue, J., Russell, J. M., and Zhang, X.: Long-term trend and solar cycle in the middle atmosphere temperature
687 revealed from merged HALOE and SABER datasets, *J. Atmos. Solar-Terrestrial Phys.*, 212, 105506,
688 <https://doi.org/10.1016/j.jastp.2020.105506>, 2021.

689 Liu, X., Yue, J., Xu, J., Garcia, R. R., Russell, J. M., Mlynczak, M., Wu, D. L., and Nakamura, T.: Variations of global
690 gravity waves derived from 14 years of SABER temperature observations, *J. Geophys. Res.*, 122, 6231–6249,
691 <https://doi.org/10.1002/2017JD026604>, 2017.

692 Lübken, F. J., Berger, U., and Baumgarten, G.: On the Anthropogenic Impact on Long-Term Evolution of Noctilucent
693 Clouds, *Geophys. Res. Lett.*, 45, 6681–6689, <https://doi.org/10.1029/2018GL077719>, 2018.

694 Lübken, F. J., Baumgarten, G., and Berger, U.: Long term trends of mesospheric ice layers: A model study, *J. Atmos.*
695 *Solar-Terrestrial Phys.*, 214, 105378, <https://doi.org/10.1016/j.jastp.2020.105378>, 2021.

696 Mlynczak, M. G., Daniels, T., Hunt, L. A., Yue, J., Marshall, B. T., Russell, J. M., Remsberg, E. E., Tansock, J., Esplin,
697 R., Jensen, M., Shumway, A., Gordley, L., and Yee, J. H.: Radiometric Stability of the SABER Instrument, *Earth*
698 *Sp. Sci.*, 7, 1–8, <https://doi.org/10.1029/2019EA001011>, 2020.

699 Mlynczak, M. G., Hunt, L. A., Garcia, R. R., Harvey, V. L., Marshall, B. T., Yue, J., Mertens, C. J., and Russell, J. M.:
700 Cooling and Contraction of the Mesosphere and Lower Thermosphere From 2002 to 2021, *J. Geophys. Res.*
701 *Atmos.*, 127, 1–17, <https://doi.org/10.1029/2022JD036767>, 2022.

702 Mlynczak, M. G., Marshall, B. T., Garcia, R. R., Hunt, L., Yue, J., Harvey, V. L., Lopez-Puertas, M., Mertens, C., and
703 Russell, J.: Algorithm stability and the long-term geospace data record from TIMED/SABER, *Geophys. Res. Lett.*,
704 50, 1–7, <https://doi.org/10.1029/2022GL102398>, 2023.

705 Picone, J. M., Hedin, A. E., Drob, D. P., and Aikin, A. C.: NRLMSISE-00 empirical model of the atmosphere:
706 Statistical comparisons and scientific issues, *J. Geophys. Res. Sp. Phys.*, 107, 1–16,
707 <https://doi.org/10.1029/2002JA009430>, 2002.

708 Qian, L., Burns, A., and Yue, J.: Evidence of the Lower Thermospheric Winter-to-Summer Circulation From SABER
709 CO₂ Observations, *Geophys. Res. Lett.*, 44, 10,100-10,107, <https://doi.org/10.1002/2017GL075643>, 2017.

710 Qian, L., Jacobi, C., and McInerney, J.: Trends and solar irradiance effects in the mesosphere, *J. Geophys. Res. Sp.*
711 *Phys.*, 124, 1343–1360, <https://doi.org/10.1029/2018JA026367>, 2019.

712 Ramesh, K., Smith, A. K., Garcia, R. R., Marsh, D. R., Sridharan, S., and Kishore Kumar, K.: Long-term variability and
713 tendencies in middle atmosphere temperature and zonal wind from WACCM6 simulations during 1850–2014, *J.*
714 *Geophys. Res. Atmos.*, 125, <https://doi.org/10.1029/2020JD033579>, 2020.

715 Randel, W. J., Garcia, R. R., Calvo, N., and Marsh, D.: ENSO influence on zonal mean temperature and ozone in the
716 tropical lower stratosphere, *Geophys. Res. Lett.*, 36, n/a-n/a, <https://doi.org/10.1029/2009GL039343>, 2009.

717 Remsberg, E. E., Marshall, B. T., Garcia-Comas, M., Krueger, D., Lingenfelter, G. S., Martin-Torres, J., Mlynczak, M.
718 G., Russell, J. M., Smith, A. K., Zhao, Y., Brown, C., Gordley, L. L., Lopez-Gonzalez, M. J., Lopez-Puertas, M.,
719 She, C. Y., Taylor, M. J., and Thompson, R. E.: Assessment of the quality of the version 1.07 temperature-versus-
720 pressure profiles of the middle atmosphere from TIMED/SABER, *J. Geophys. Res. Atmos.*, 113, 1–27,
721 <https://doi.org/10.1029/2008JD010013>, 2008.

722 Rezac, L., Kutepov, A., Russell, J. M., Feofilov, A. G., Yue, J., and Goldberg, R. A.: Simultaneous retrieval of T(p) and
723 CO₂ VMR from two-channel non-LTE limb radiances and application to daytime SABER/TIMED measurements,
724 *J. Atmos. Solar-Terrestrial Phys.*, 130–131, 23–42, <https://doi.org/10.1016/j.jastp.2015.05.004>, 2015.

725 Russell, J. M., Bailey, S. M., Gordley, L. L., Rusch, D. W., Horányi, M., Hervig, M. E., Thomas, G. E., Randall, C. E.,
726 Siskind, D. E., Stevens, M. H., Summers, M. E., Taylor, M. J., Englert, C. R., Espy, P. J., McClintock, W. E., and
727 Merkel, A. W.: The Aeronomy of Ice in the Mesosphere (AIM) mission: Overview and early science results, *J.*
728 *Atmos. Solar-Terrestrial Phys.*, 71, 289–299, <https://doi.org/10.1016/j.jastp.2008.08.011>, 2009.

729 She, C. Y., Berger, U., Yan, Z., Yuan, T., Lübken, F. -J., Krueger, D. A., and Hu, X.: Solar response and long-term
730 trend of midlatitude mesopause region temperature based on 28 years (1990–2017) of Na lidar observations, *J.*
731 *Geophys. Res. Sp. Phys.*, 124, 7140–7156, <https://doi.org/10.1029/2019JA026759>, 2019.

732 Tapping, K. F.: The 10.7 cm solar radio flux (F 10.7), *Sp. Weather*, 11, 394–406, <https://doi.org/10.1002/swe.20064>,
733 2013.

734 Venkat Ratnam, M., Akhil Raj, S. T., and Qian, L.: Long-Term Trends in the Low-Latitude Middle Atmosphere
735 Temperature and Winds: Observations and WACCM-X Model Simulations, *J. Geophys. Res. Sp. Phys.*, 124,
736 7320–7331, <https://doi.org/10.1029/2019JA026928>, 2019.

737 Wang, N., Qian, L., Yue, J., Wang, W., Mlynczak, M. G., and Russell, J. M.: Climatology of mesosphere and lower
738 thermosphere residual circulations and mesopause height derived from SABER observations, *J. Geophys. Res.*
739 *Atmos.*, 127, 1–14, <https://doi.org/10.1029/2021JD035666>, 2022.

740 Xu, J., Liu, H. L., Yuan, W., Smith, A. K., Roble, R. G., Mertens, C. J., Russell, I. M., and Mlynczak, M. G.:
741 Mesopause structure from Thermosphere, Ionosphere, Mesosphere, Energetics and Dynamics (TIMED/Sounding
742 of the Atmosphere Using Broadband Emission Radiometry (SABER) observations, *J. Geophys. Res. Atmos.*, 112,
743 <https://doi.org/10.1029/2006JD007711>, 2007.

744 Yu, W., Garcia, R., Yue, J., Smith, A., Wang, X., Randel, W., Qiao, Z., Zhu, Y., Harvey, V. L., and Tilmes, S.:
745 Mesospheric Temperature and Circulation Response to the Hunga Tonga-Hunga-Ha ’apai Volcanic Eruption
746 *Journal of Geophysical Research : Atmospheres*, 1–10, <https://doi.org/10.1029/2023JD039636>, 2023.

747 Yuan, T., Solomon, S. C., She, C. -Y., Krueger, D. A., and Liu, H. -L.: The long-term trends of nocturnal mesopause
748 temperature and altitude revealed by Na lidar observations between 1990 and 2018 at midlatitude, *J. Geophys. Res.*
749 *Atmos.*, 124, 5970–5980, <https://doi.org/10.1029/2018JD029828>, 2019.

750 Yue, J., Russell, J., Jian, Y., Rezac, L., Garcia, R., López-Puertas, M., and Mlynczak, M. G.: Increasing carbon dioxide
751 concentration in the upper atmosphere observed by SABER, *Geophys. Res. Lett.*, 42, 7194–7199,
752 <https://doi.org/10.1002/2015GL064696>, 2015.

753 Yue, J., Russell, J., Gan, Q., Wang, T., Rong, P., Garcia, R., and Mlynczak, M.: Increasing water vapor in the
754 stratosphere and mesosphere after 2002, *Geophys. Res. Lett.*, 46, 13452–13460,
755 <https://doi.org/10.1029/2019GL084973>, 2019a.

756 Yue, J., Li, T., Qian, L., Lastovicka, J., and Zhang, S.: Introduction to special issue on “Long-term changes and trends
757 in the middle and upper atmosphere,” *J. Geophys. Res. Sp. Phys.*, 124, 10360–10364,
758 <https://doi.org/10.1029/2019JA027462>, 2019b.

759 Zhang, S., Cnossen, I., Laštovička, J., Elias, A. G., Yue, X., Jacobi, C., Yue, J., Wang, W., Qian, L., and Goncharenko,
760 L.: Long-term geospace climate monitoring, *Front. Astron. Sp. Sci.*, 10, 1–5,
761 <https://doi.org/10.3389/fspas.2023.1139230>, 2023.

762 Zhao, X. R., Sheng, Z., Shi, H. Q., Weng, L. B., and Liao, Q. X.: Long-Term Trends and Solar Responses of the
763 Mesopause Temperatures Observed by SABER During the 2002–2019 Period, *J. Geophys. Res. Atmos.*, 125, 1–17,
764 <https://doi.org/10.1029/2020JD032418>, 2020.

765 Zhao, X. R., Sheng, Z., Shi, H. Q., Weng, L. B., and He, Y.: Middle atmosphere temperature changes derived from
766 SABER observations during 2002–2020, *J. Clim.*, 34, 1, <https://doi.org/10.1175/JCLI-D-20-1010.1>, 2021.

767